Dynamic fracture-path prediction in impact fracture phenomena using moving finite element method based on Delaunay automatic mesh generation

Nishioka, Toshihisa

Tokudome, Hiroyuki

Kinoshita, Masahiro

Dynamic Fracture-Path Prediction in Impact Fracture Phenomena Using Moving Finite Element Method Based on Delaunay Automatic Mesh Generation

Toshihisa NISHIOKA*, Hiroyuki TOKUDOME** and Masahiro KINOSHITA**

*Corresponding Author
    Professor
    Department of Ocean Mechanical Engineering,
    Kobe University of Mercantile Marine
    5-1-1 Fukae Minamimachi, Higashinada-ku, Kobe, 658-0022, Japan
    TEL & FAX: +81-78-431-6282
    E-mail: nishioka@cc.kshosen.ac.jp

**   Graduate Student
    Department of Ocean Mechanical Engineering,
    Kobe University of Mercantile Marine
    5-1-1 Fukae Minamimachi, Higashinada-ku, Kobe, 658-0022, Japan

Abstract

First, this paper presents the concept of mixed-phase simulation with fracture-path prediction mode which uses a postulated propagation-direction criterion together with experimentally obtained crack-propagation history. Furthermore, this paper presents the development of an automatic moving finite element method that incorporates the Delaunay automatic triangulation. Using the automatic moving finite element method, the mixed-phase simulation with fracture-path prediction mode is carried out for mixed-mode impact fracture tests. Various dynamic fracture mechanics parameters are evaluated by the path-independent dynamic J integral. The moving finite element method in conjunction with the local symmetry (K_{II}=0) criterion successfully predicts the numerical fracture path in excellent agreement with experimentally obtained actual fracture path.

Key Words: Dynamic Fracture, Impact Fracture, Dynamic Fracture Mechanics, Dynamic Crack Propagation, Dynamic Crack Kinking, Dynamic Crack Curving, Delaunay Automatic Triangulation, Moving Element Method, Dynamic J Integral, Path Prediction Mode

1. Introduction

Numerical prediction of dynamic fracture path is an extremely important research subject not only for academic interest (Nishioka, 1994 and 1997) but also for the establishment of a safety design methodology that prevents catastrophic overall failures of structures. However, numerical fracture-path predictions of non-self-similar dynamic fracture phenomena have not been succeeded until recently, due to various inherent difficulties.

To establish the numerical methodology for dynamic fracture path prediction, first, Nishioka et al. (1990b) have developed a moving finite element method based on a mapping technique. Using this moving finite element method, they have carried out the generation-phase simulation of fast

curving fracture in double cantilever beam (DCB) specimens (Nishioka et al., 1990a). Next, Nishioka (1997) has proposed the concept of "mixed phase simulation" together with "fracture-path prediction mode" and "crack-growth prediction mode". Then, using the moving finite element method based on the mapping technique, the mixed-phase simulation with the fracture-path prediction mode has been carried out (Nishioka et al., 1996 and 1997) for dynamically curving crack propagation in the DCB specimens. The moving finite element simulation has succeeded to predict the experimentally obtained actual fracture paths.

However, the dynamic fracture paths in the DCB specimens under static loading were rather smooth. The moving finite element method based on the mapping technique may be somewhat difficult to apply to the problems of dynamic crack kinking and dynamic crack branching.

In the this study, to establish a simulation method for complex crack propagation, a moving finite element method based on Delaunay automatic triangulation (Sloan and Houlsby, 1992, and Taniguchi, 1992) is developed. Furthermore, the present moving finite element method is combined with the concept of the mixed-phase simulation with fracture-path prediction mode. The moving finite element method based on Delaunay automatic triangulation successfully demonstrates the prediction of dynamic fracture paths in mixed-mode impact fracture experiments

2. Mixed-Mode Impact Fracture Experiments

The geometry of a three-point bend specimen for mixed-mode impact fracture test is shown in Fig.1. The dimensions of the specimen are as follows; length L=430 mm, width W=100 mm, span S=400 mm, thickness h=10 mm, and initial crack length a_0=50mm. Polymethyl methacrylate (PMMA) was used in the present experiment. The material properties are Young's modulus E=2.94 Gpa, Poisson's ratio ν=0.3, mass density ρ=1190 kg/m^3. The longitudinal (dilatational) and shear wave velocities in this material are C_d=1710 m/s and C_s=941 m/s, respectively.

The initial crack consists of a machine notch of 35 mm and a fatigue crack of 15 mm. The impact load by a dropping rod (5.05 Kg) was applied at the off-center point as shown in Fig.1. The initial impact velocity of the hammer was set as 5 m/s. The loading eccentricity is defined as e=l/(S/2). To induce various magnitudes of mixed-mode state in the specimen, the loading eccentricity was systematically changed.

Figure 2 shows a photograph of the specimens fractured by the impact loading with e=0.0, 0.1, 0.2, 0.3, 0.4 and 0.5. The kinked angle from the initial crack tip systematically increases with increasing loading eccentricity. The dynamic fracture paths are fairly smooth, and propagate toward the corresponding loading points.

High-speed photographs of dynamic fracture events were taken by using a laser caustic method and a high-speed camera. The high-speed photographs of dynamically fracturing specimen under the loading eccentricity of e=0.0 are shown in Fig.3. The time intervals of the photographs are about 30 μs. After the impact loading was applied, the caustic patterns of the mode I (crack opening mode) around the crack tip became larger until the time of the photograph (7). At the time of the photograph (8), the crack had already propagated for a short distance. Then, it is seen in the photograph (16) that the specimen almost completely broke into two parts.

Figure 4 shows the high-speed photographs of the dynamically fracturing specimen under the loading eccentricity of e=0.1. In the photographs (4), (5) and (6), the caustic patterns of the mode II (in-plane shearing mode) dominated type can be seen. At the time of the photograph (7), the crack had already propagated for a short distance. The caustic pattern in the photograph (7) suddenly changed to mode I dominated type. The specimen almost completely broke into two parts at the time of the photograph (15). Around the initial crack tip, a caustic pattern due to a bending moment can be seen in the right-hand side of specimen in the photographs (15) and (16).

For both specimens, the caustic patterns due to the impact loading are always seen under the impact rod, except in the first photographs. This implies that the specimens were always pushed after the impact loading. Thus the loading rod was in contact with the specimen throughout the fracture test.

Crack propagation histories measured by the caustics in the high-speed photographs are shown

in Figs.5 and 6. Dynamic fracture occurred at t=156 μs in the specimen of e=0.0, and at t=120 μs in the specimen of e=0.1, respectively. The maximum crack velocity observed was about 250 m/s in the specimen of e=0.0, and about 300 m/s in the specimen of e=0.1, respectively.

On the basis of a theory of mixed-mode dynamic caustics (Nishioka and Kittaka, 1990), the characteristic dimensions of the caustic patterns were converted to dynamic stress intensity factors (see Figs.25 and 26).

3. Types of Simulation for Fracture Phenomena

For non-self-similar fracture such as curving crack growth, three types of numerical simulation have been proposed by Nishioka (1997), as explained in Fig.7. Here, we consider a dynamic curving fracture problem as an example. In Fig.7, symbols a, C ($\equiv \dot{a}$), J' and t denote the crack length, crack velocity, dynamic J integral, and time, respectively. The curve in the global coordinate system (X_1, X_2) represents the curved fracture path.

Suppose that the specimen is modeled by a numerical analysis method such as the finite element method. To this end, all dimensions of the specimen should be prescribed. In addition the material behavior and the initial and boundary conditions should be known.

In the generation phase simulation, the fracture test is reproduced in the computer model using the experimentally measured crack propagation history (a versus t or C versus t) and the curved fracture-path history (see Fig.7(i)). The generation phase simulation was originally proposed by Kanninen (1978) for self-similar (linearly propagating) fracture problems. In this simulation, fracture parameters such as the dynamic J integral and the dynamic stress intensity factors can be evaluated during dynamic fracture processes. From this calculation, one can determine the fracture toughness as the material resistance against the fracture initiation, crack propagation and crack arrest (if any). Then, one may postulate various fracture criteria based on the information obtained by the generation phase simulation.

On the other hand, in the application phase simulation for curving crack growth, two criteria must be postulated or predetermined as shown in Fig.7(ii). One is a crack-propagation criterion that determines the crack increment or the crack velocity at each time step. Other one is a criterion for predicting the direction of crack propagation (propagation-direction criterion or growth-direction criterion). In this simulation, the crack propagation history (a versus t or C versus t) and the fracture-path history are used to produce a virtual reality fracture in the computational model. The application phase simulation is also sometimes called "prediction" or "inverse" simulation.

However, the application phase simulations of curving crack growth have not been fully established, due to several critical difficulties in those simulations. For instance, in dynamic brittle fracture, the crack-propagation criterion described by fracture-toughness versus crack-velocity relation itself has several unsolved problems. The stress intensity factor during dynamic crack propagation depends on not only the crack velocity but also the crack acceleration (Takahashi and Arakawa, 1987). Furthermore, the crack-propagation criteria may also be influenced by the geometry of fracture specimen.

To verify only the propagation-direction criterion such as the maximum energy release rate criterion, Nishioka (1997) has proposed "mixed-phase simulation" as depicted in Fig.7(iii-a). Regarding the crack-propagation history, the same experimental data for the a-t relation used in the generation phase simulation are used. Thus, the increment of crack propagation is prescribed for the given time increment in the numerical simulation. Then the propagation-direction criterion predicts the direction of fracture path at each time step. Simulated final fracture path will be compared with the actual one obtained by the experiment. This mode of the mixed-phase simulation is called as "fracture-path prediction mode" (see Fig.7(iii-a)).

Another mode of the mixed-phase simulation can be considered as depicted in Fig.7(iii-b), i.e., "crack-growth prediction mode". In this mode, the experimental data for the fracture-path history and a crack-propagation criterion are used simultaneously. In this case, the crack is forced to propagate along the actual fracture path during the numerical simulation. Simulated crack-propagation history should agree with the experimentally obtained actual one if the postulated

crack-propagation criterion is valid.

As explained above, using the mixed-phase simulation, the crack-propagation criterion and the propagation-direction criterion can be verified separately. The concept of mixed-phase simulation can also be applied to curving fatigue crack growth and curving stable crack growth.

4. Moving Finite Element Method Based on Delaunay Automatic Mesh Generation

In a dynamic crack propagation problem, the crack surfaces that are usually free surfaces extend with a high velocity, and the stresses and strains at the crack tip or at the crack front become unbounded. Consequently, one must solve a moving singular-point boundary-value problem. The high-velocity moving singular point usually induces various numerical errors in the computational model. Therefore, a highly accurate numerical analysis method is mandatory to solve the dynamic crack propagation problem.

To simulate the crack propagation by the finite element method, two different concepts of computational modeling can be considered, i.e., (i) the stationary element procedure (or fixed element procedure), and (ii) the moving element procedure, as reviewed by Nishioka and Atluri (1986), and Nishioka (1994 and 1997). For self-similar dynamic crack propagation problems, it is well known that the numerical results of the moving element procedure are generally more accurate than those of the fixed element procedure. However, the moving element procedure was difficult to apply to non-self-similar dynamic crack propagation problems except for smoothly curving fracture problems (Nishioka et al., 1996 and 1997), because of the difficulties in moving the near-tip elements along curved or kinked path.

In order to overcome the aforementioned difficulties, a moving finite element method based on Delaunay automatic mesh generation is developed in this study. A crack growth procedure combining automatic mesh generation was also developed by Camacho and Ortiz (1996). However, their method falls into the category of the fixed element procedure.

4.1 Modified Delaunay automatic triangulation

Delaunay triangulation (Sloan and Houlsby, 1984) automatically generates triangles that cover the whole area within an arbitrarily specified convex region. All generated triangular elements do not contain any other nodes within their circumscribed circles. This feature is also preferable to the triangular finite elements from an accuracy point of view.

Taniguchi (1992) has developed the modified Delaunay triangulation which can treat a concave region such a cracked body. He has also developed a program for automatic mesh generation on the basis of the modified Delaunay triangulation (Taniguchi, 1992). The remeshing procedure in the modified Delaunay triangulation is shown in Fig.8. If a flat element has a large interior angle, then the triangular elements around it are remeshed as shown in Fig.8. In this procedure, the new nodal point is placed at the mid-point of the opposite side of the maximum interior angle.

In the modified Delaunay triangulation, only exterior and interior boundary points and specified interior points (if they are necessary) are required for automatic mesh generation. Figure 9 shows an example of mesh generation for a plate with an edge crack. The specified points at the boundaries are shown in Fig.9(a). To distinguish the upper and lower crack surfaces, the coordinates of the upper and lower crack surfaces are shifted by infinitesimally small distances $\pm\varepsilon$ in the perpendicular direction to the crack surfaces. Thus, the crack is opened by 2 ε. Due to the stress singularity at the crack tip, the specified interior points are placed around the crack tip as depicted in Fig.9(b). The mesh pattern in Fig.9(c) is automatically generated using the exterior boundary points and the specified interior points.

4.2 Automatic mesh generation for a propagating crack

Nishioka and coworkers have developed various types of moving finite element procedure. These are reviewed and summarized by Nishioka and Atluri (1986) and Nishioka (1994 and 1997). In this study, the concept of the moving finite element method is extended to complex crack

4

propagation problems using the modified Delaunay automatic triangulation.

In the moving finite element method based on Delaunay automatic triangulation, a crack is advanced as shown in Fig.10. The group of the specified interior points around the propagating crack tip translates in each time step for which crack growth occurs. In each time step, the previous crack tip point breaks into two nodal points. In this study, the number of exterior boundary points is increased by two for each time step during crack propagation. Thus at least four degrees of freedom should be increased in each crack increment. The crack-tip always remains at the center of the group of the moving elements throughout the analysis even for complicated crack propagation. At each time step, the interior region between the specified nodes around the crack tip and the specified boundary nodes, is automatically broken into triangular elements by using the modified Delaunay automatic triangulation.

4.3 Time integration method

In this study, the Newmark method is used for the time integration of the finite element equations of motion. At a generic time step n, the final simultaneous equations to be solved are expressed as

$$\left(a_0[M]^{(n)}+[K]^{(n)}\right)\{Q\}_n^{(n)}=\{F\}_n^{(n)}+[M]^{(n)}\left(a_0\{Q\}_{n-1}^{(n)}+a_2\{\dot{Q}\}_{n-1}^{(n)}+a_3\{\ddot{Q}\}_{n-1}^{(n)}\right) \tag{1}$$

where $\{Q\}$, $\{\dot{Q}\}$, $\{\ddot{Q}\}$ are the global vectors of nodal displacements, nodal velocities and nodal accelerations, respectively. The subscripts n and n-1 denote the quantities at the present time step n and at the previous time step n-1, respectively, while the superscript (n) denotes the quantities in the mesh pattern of the present time step n. [M], [K], {F} are the mass matrix, the stiffness matrix and the load vector, respectively. The coefficients $a_0 \sim a_3$ are the parameters in the Newmark method (see Eq.(4)).

After solving Eq.(1) for the nodal displacements at the present time step, the nodal velocities and accelerations can be evaluated by the following equations:

$$\{\ddot{Q}\}_n^{(n)}=a_0\left(\{Q\}_n^{(n)}-\{Q\}_{n-1}^{(n)}\right)-a_2\{\dot{Q}\}_{n-1}^{(n)}-a_3\{\ddot{Q}\}_{n-1}^{(n)}, \tag{2}$$

$$\{\dot{Q}\}_n^{(n)}=\{\dot{Q}\}_{n-1}^{(n)}+a_6\{\ddot{Q}\}_{n-1}^{(n)}+a_7\{\ddot{Q}\}_n^{(n)}. \tag{3}$$

The coefficients are given as

$$a_0=\frac{1}{\beta(\Delta t_n)^2}, \quad a_1=\frac{\delta}{\beta\Delta t_n}, \quad a_2=\frac{1}{\beta\Delta t_n}, \quad a_3=\frac{1}{2\beta}-1, \quad a_4=\frac{\delta}{\beta}-1, \quad a_5=\frac{\Delta t_n}{2}\left(\frac{\delta}{\beta}-2\right), \quad a_6=\Delta t_n(1-\delta), \quad a_7=\delta\Delta t_n \tag{4}$$

where Δt_n is the time increment at the present time step. In this study, the Newmark's parameters are chosen to be $\beta=1/4$ and $\delta=1/2$ to fulfill the unconditionally stable condition (Bathe and Wilson, 1976).

4.4 Mapping of solution fields in the previous mesh onto those in the present mesh

As explained in the previous subsections, in the moving finite element method, the moving-mesh and remeshing procedures are used (see Fig.10). To use the Newmark time integration scheme for the moving finite element method, the previous solution fields for the current mesh pattern are needed, i.e., $\{Q\}_{n-1}^{(n)}$, $\{\dot{Q}\}_{n-1}^{(n)}$, $\{\ddot{Q}\}_{n-1}^{(n)}$ (see the right-hand side of Eq.(1)). This means that the mapping of the solution fields in the previous mesh onto those in the present mesh is needed.

In this subsection, the detailed procedures for constructing $\{Q\}_{n-1}^{(n)}$, $\{\dot{Q}\}_{n-1}^{(n)}$, $\{\ddot{Q}\}_{n-1}^{(n)}$ from the previous solution fields in the previous mesh $\{Q\}_{n-1}^{(n-1)}$, $\{\dot{Q}\}_{n-1}^{(n-1)}$ and $\{\ddot{Q}\}_{n-1}^{(n-1)}$ are given. For the mapping of the solution fields in the previous mesh onto those in the present mesh, we have developed the following two procedures.

(1) Searching an element in the previous mesh for a new nodal point

Let us consider a newly created nodal point in the present mesh as the pth node. The program searches the element in the previous mesh in which the new pth node is included, as shown in Fig.11. The triangles A_1, A_2 and A_3 are calculated by the following determinants:

5

$$A_1 = \frac{1}{2} \begin{vmatrix} 1 & x_p & y_p \\ 1 & x_2 & y_2 \\ 1 & x_3 & y_3 \end{vmatrix} = 0.5 \{x_2 y_3 - x_3 y_2 + (y_2 - y_3)x_p + (x_3 - x_2)y_p\}, \tag{5.a}$$

$$A_2 = \frac{1}{2} \begin{vmatrix} 1 & x_p & y_p \\ 1 & x_3 & y_3 \\ 1 & x_1 & y_1 \end{vmatrix} = 0.5 \{x_3 y_1 - x_1 y_3 + (y_3 - y_1)x_p + (x_1 - x_3)y_p\}, \tag{5.b}$$

$$A_3 = \frac{1}{2} \begin{vmatrix} 1 & x_p & y_p \\ 1 & x_1 & y_1 \\ 1 & x_2 & y_2 \end{vmatrix} = 0.5 \{x_1 y_2 - x_2 y_1 + (y_1 - y_2)x_p + (x_2 - x_1)y_p\}. \tag{5.c}$$

where x_p and y_p are the coordinates of the point p, and x_i and y_i (i=1,2,3) are the coordinates of the nodes 1, 2 and 3.

It can easily be judged whether the pth node is inside of the element or not. If A_1, A_2 and A_3 are all positive, the pth node is inside of the element, while it is outside if any of A_1, A_2 or A_3 is negative.

(2) Creating nodal quantities for the new nodal point

Once the old element including the new pth node is found, the area coordinates of the pth node can be calculated by

$$\xi_{1p} = A_1 / A_e, \quad \xi_{2p} = A_2 / A_e, \quad \xi_{3p} = A_3 / A_e \tag{6}$$

where A_e is the area of the element. Since in this paper we use linear triangle elements, the shape functions N_i of the point p are given by

$$N_i = \xi_{ip} \ (i=1, 2, 3). \tag{7}$$

Using these shape functions, the nodal displacements, nodal velocities and nodal accelerations in the x and y directions can be constructed for the new pth node as follows:

$$\left(u_p\right)_{n-1}^{(n)} = \sum_{i=1}^{3} N_i^{(n-1)}\left(\xi_{1p}, \xi_{2p}, \xi_{3p}\right) \left(u_i\right)_{n-1}^{(n-1)}; \ (p=1,2 \cdots N) \tag{8.a}$$

$$\left(v_p\right)_{n-1}^{(n)} = \sum_{i=1}^{3} N_i^{(n-1)}\left(\xi_{1p}, \xi_{2p}, \xi_{3p}\right) \left(v_i\right)_{n-1}^{(n-1)}; \ (p=1,2 \cdots N) \tag{8.b}$$

$$\left(\dot{u}_p\right)_{n-1}^{(n)} = \sum_{i=1}^{3} N_i^{(n-1)}\left(\xi_{1p}, \xi_{2p}, \xi_{3p}\right) \left(\dot{u}_i\right)_{n-1}^{(n-1)}; \ (p=1,2 \cdots N) \tag{9.a}$$

$$\left(\dot{v}_p\right)_{n-1}^{(n)} = \sum_{i=1}^{3} N_i^{(n-1)}\left(\xi_{1p}, \xi_{2p}, \xi_{3p}\right) \left(\dot{v}_i\right)_{n-1}^{(n-1)}; \ (p=1,2 \cdots N) \tag{9.b}$$

$$\left(\ddot{u}_p\right)_{n-1}^{(n)} = \sum_{i=1}^{3} N_i^{(n-1)}\left(\xi_{1p}, \xi_{2p}, \xi_{3p}\right) \left(\ddot{u}_i\right)_{n-1}^{(n-1)}; \ (p=1,2 \cdots N) \tag{10.a}$$

$$\left(\ddot{v}_p\right)_{n-1}^{(n)} = \sum_{i=1}^{3} N_i^{(n-1)}\left(\xi_{1p}, \xi_{2p}, \xi_{3p}\right) \left(\ddot{v}_i\right)_{n-1}^{(n-1)}; \ (p=1,2 \cdots N) \tag{10.b}$$

where N denotes the total number of new nodes created in the remeshed zone including the moving element zone.

5. Contact and Non-Contact Boundary Conditions for Loading and Support Points

Since in general the impact rod and the supports in the three-point bend test can "push" the specimen but not "pull" (see Fig.1), the fixed boundary conditions at the loading point and at the supports in the numerical analysis may lead to a spurious deformation behavior of the specimen. Thus, account should be taken of the possibility of lack of contact of the specimen with each of the impact rod, the left, or right support at various instants of time. For this kind of problem, Nishioka and coworkers were the first to introduce the contact/non-contact boundary conditions to three-point bend specimens (Nishioka and Atluri, 1982), and to double cantilever beam specimens (Nishioka et

al., 1982). From the numerical results for the three-point bend fracture test (Nishioka et al., 1983), it was found that the specimen was periodically not in contact with either the impact rod or the supports; i.e. the specimen periodically became a free-flying object.

In the present study, the contact/non-contact boundary conditions are also employed in the numerical simulations. The contact/non-contact boundary conditions are incorporated in the program as follows.

We designate the nodal forces at the impact loading point, the left and right supports as $F_{X\alpha}$ (α=h, l, r) (the global X direction is taken in parallel with the initial crack direction), and the corresponding displacement components at those points as u_α (α=h, l, r). Then, those nodal forces and displacements in the next time step (n+1) are predicted by

$$(F_{X\alpha})_{n+1} = (F_{X\alpha})_n + \frac{((F_{X\alpha})_n - (F_{X\alpha})_{n-1})}{\Delta t_n} \Delta t_{n+1}: (\alpha=h, l, r) \tag{11}$$

and

$$(u_\alpha)_{n+1} = (u_\alpha)_n + (\dot{u}_\alpha)_n \Delta t_{n+1}: (\alpha=h, l, r). \tag{12}$$

The initial conditions at those points are given by

$$(u_\alpha)_0 = (\bar{u}_\alpha)_0, \ (\dot{u}_\alpha)_0 = (\dot{\bar{u}}_\alpha)_0, \ (\ddot{u}_\alpha)_0 = (\ddot{\bar{u}}_\alpha)_0: (\alpha=h, l, r) \tag{13}$$

where the upper bars denote prescribed values. In this study, since the mass of the specimen is fairly small (0.512 Kg) compared with that of the rod (5.05 Kg), and since the duration of the impact load is very short, the velocity of the rod is assumed to be constant i.e., $(\dot{\bar{u}}_h)_n$ = 5 m/s throughout the analysis. Thus, the displacement and acceleration of the rod are given by $(\bar{u}_h)_n = (\dot{\bar{u}}_h)_0 \times t$ and $(\ddot{\bar{u}}_h)_n$ = 0, respectively. The positions of the supports are fixed throughout the analysis, as $(\bar{u}_\beta)_n = (\dot{\bar{u}}_\beta)_n = (\ddot{\bar{u}}_\beta)_n = 0$ (β=l, r).

A negative value of $(F_{Xh})_{n+1}$ indicates that the specimen will be pushed by the impact rod, while a positive value of $(F_{X\beta})_{n+1}$ (β=l, r) indicates that the specimen will be pushed by the supports. Thus, the contact condition at each point continues if the sign of the corresponding predicted nodal force at the next time step (n+1) (see Eq.(11)) remains unchanged. The non-contact condition at each point occurs if the corresponding value of $(F_{X\alpha})_{n+1}$ (α=h, l, r) becomes zero or of the different sign.

When the non-contact condition is predicted, that point is set as free at the next time step. The movement of that point is calculated by the simulation. The free state continues if the sign of the gap $((u_\alpha)_{n+1} - (\bar{u}_\alpha)_{n+1})$ (α=h, l, r) remains unchanged from the current time step. Then, re-contact condition occurs if the gap $((u_\alpha)_{n+1} - (\bar{u}_\alpha)_{n+1})$ (α=h, l, r) is predicted as zero or of the different sign.

Although in (Nishioka et al., 1983) the time increment was subdivided whenever the transition to the non-contact or re-contact condition was predicted to occur prior to the time of the next step, in this study a sufficiently small constant time increment is always used throughout the simulation.

6. Fracture-Path Prediction Procedure

As explained in Section 3, in the mixed-phase fracture-path prediction mode simulation, a propagation-direction criterion is needed to be postulated. Many criteria have been proposed in literature. Some of these criteria are listed below:

(i) maximum hoop stress criterion ($\sigma_{\theta\theta}$ max) (Erdogan and Sih, 1963),

(ii) minimum strain energy density criterion (S min) (Sih, 1972),

(iii) maximum second stress invariant criterion (I_2 max) (Papadopoulos, 1988),

(iv) maximum stress intensity factor criterion (K_I max) (Nemat-Nasser and Horii, 1982),

(v) maximum energy release rate criterion (G max) (Wu, 1978),

(vi) local symmetry criterion (K_{II} =0) (Goldstein and Salganik, 1974).

Furthermore, these criteria can be classified into (a) explicit prediction theory and (b) implicit prediction theory. An explicit prediction theory predicts the propagation direction satisfying the postulated criterion based on a physical quantity for the current crack tip. Then, the crack is advanced in this direction, with a small crack-length increment according to the experimental crack-propagation history. The criteria (i), (ii) and (iii) fall into this category.

Contrary to this, an implicit prediction theory seeks the propagation direction that satisfies the

7

postulated criterion based on a physical quantity after the crack is advanced with a small crack-length increment. An iterative process is generally needed to find the propagation direction. The criteria (iv), (v) and (vi) are classified into this category. It is known that in general the implicit prediction theories are more accurate.

Nishioka et al. (1996 and 1997) have succeeded to predict a smooth fast curving fracture path in a DCB specimen, using the moving isoparametric element method based on the mapping technique. In the previous studies (Nishioka et al., 1996 and 1997), the criteria (iv)-(vi) were tested in the mixed-phase simulation with the fracture-path prediction mode. It was found from these simulations that the predicted fracture path based on the local symmetry criterion most accurately agreed with the actual experimental fracture path. Thus, in this section, numerical procedures based on only the local symmetry criterion are explained. However, all implicit criteria as well as all explicit criteria can be tested in a similar manner if they are well described in terms of physical quantities.

Figure 12 schematically explains the numerical procedures for the path-prediction mode of the mixed-phase simulation. In each time step, the crack is advanced by a small increment according to the experimental history (crack-length versus time curve).

The fracture path is predicted in an iterative manner as follows: In the following a superscript (i) denotes the iteration number. At a generic time step n, as the first trial, the crack is advanced in the tangential direction $\theta_n^{(i)}$ (i=1) at the crack tip of the step n-1. If an employed propagation-direction criterion, for example the local symmetry (K_{II}=0) criterion, is satisfied at the attempted crack-tip location, the crack is advanced in this direction $\theta_n^{(i)}$. If the K_{II} value is negative, the crack is tentatively advanced in the direction of $\theta_n^{(i+1)}=\theta_n^{(i)}+\Delta\theta$, as the next trial. If the K_{II} value is positive, $\Delta\theta$ is taken as negative. Then, the satisfaction of the criterion at the trial crack tip location is checked. If the criterion is not satisfied and the value of the K_{II} value at the present trial is different with that at the previous trial, the next trial direction $\theta_n^{(i+1)}$ that satisfies the employed propagation-direction criterion is predicted by the K_{II} versus θ curve as shown in Fig.12. If the predicted angle θ_c largely differs from the trial angle of the current iteration $\theta_n^{(i)}$, the next trial direction is taken as $\theta_n^{(i+1)}=\theta_n^{(i)}+\Delta\theta$. The crack is advanced in this direction and the satisfaction of the criterion is checked. These procedures are repeated until the criterion is satisfied. At each iteration, re-meshing is needed if the implicit criterion is used, as explained above.

After finding the propagation direction that exactly satisfies the postulated criterion, the time step proceeds to the next step.

7. Evaluation Method of Dynamic Fracture Mechanics Parameters

In this study, to evaluate various fracture mechanics parameters for a crack subject to impact stress wave loading, and for a dynamically kinking as well as dynamically curving crack, the path independent dynamic J integral derived by Nishioka and Atluri (1983) is used.

7.1 Path independent dynamic J integral

The static J integral (Rice, 1968) has played an important role in *static fracture mechanics*. From the theoretical and computational points of view, the static J integral has the following salient features: (i) it physically represents the energy release rate; (ii) it has the property of the path-independent integral, which gives a unique value for an arbitrary integral path surrounding the crack tip; (iii) it can be related to the stress intensity factors by arbitrarily shrinking the integral path to the crack tip.

In the case of *dynamic fracture mechanics*, Nishioka and Atluri (1983) have derived the dynamic J integral (J') which has the aforementioned three features. We consider a dynamically propagating crack in an elastic solid as shown in Fig.13. The global-axis components of the dynamic J integral can be expressed by

$$J'_k = \lim_{\varepsilon \to 0} \int_{\Gamma_\varepsilon} [(W+K)n_k - t_i u_{i,k}]dS \tag{14.a}$$

$$=\lim_{\varepsilon\to 0}\left\{\int_{\Gamma+\Gamma_c}[(W+K)n_k-t_iu_{i,k}]dS +\int_{V_\Gamma-V_\varepsilon}[(\rho\ddot{u}_i-f_i)u_{i,k}-\rho\dot{u}_i\dot{u}_{i,k}]dV\right\}$$ (14.b)

where u_i, t_i, f_i, n_k and ρ denote the displacement, traction, body force, outward direction cosine, and mass density, respectively. W and K are the strain and kinetic energy densities, respectively, and $(\ )_{,k}=\partial(\ )/\partial X_k$. The integral paths are defined in Fig.13. Γ_ε, Γ, and Γ_c denote a near-field path, far-field path and crack surface path, respectively. V_Γ is the region surrounded by Γ, while V_ε is the region surrounded by Γ_ε.

The crack-axis components of the dynamic J integral can be evaluated by the following coordinate transformation:

$$J'^0_l = \alpha_{lk}(\theta_0) J'_k.$$ (15)

where α_{lk} is the coordinate transformation tensor. The tangential component of the dynamic J integral J'^0_1 corresponds to the rate of change in the potential energy per unit crack extension, namely, the dynamic energy release rate.

The dynamic J integral can be related to the instantaneous stress intensity factors for the elastodynamically propagating crack with velocity C, as in (Nishioka and Atluri, 1983):

$$J'^0_1 = \frac{1}{2\mu}\left\{A_I(C)K_I^2 + A_{II}(C)K_{II}^2 + A_{III}(C)K_{III}^2\right\}$$ (16)

$$J'^0_2 = -\frac{A_{IV}(C)}{\mu}K_IK_{II}$$ (17)

where μ is the shear modulus, and $A_I(C)$-$A_{IV}(C)$ are functions of crack velocity C and given by

$$A_I(C)=\beta_1(1-\beta_2^2)/D(C), \quad A_{II}(C)=\beta_2(1-\beta_2^2)/D(C), \quad A_{III}(C)=1/\beta_2$$ (18.a,b,c)

$$A_{IV}(C)=\frac{(\beta_1-\beta_2)(1-\beta_2^2)}{\{D(C)\}^2}\left[\frac{\{4\beta_1\beta_2+(1+\beta_2^2)^2\}(2+\beta_1+\beta_2)}{2[(1+\beta_1)(1+\beta_2)]^{1/2}}-2(1+\beta_2^2)\right]$$ (18.d)

and

$$D(C)=4\beta_1\beta_2-(1+\beta_2^2)^2.$$ (19)

In the above equations, β_1 and β_2 are crack velocity parameters and defined by

$$\beta_1 =(1-C^2/C_d^2)^{1/2}, \quad \beta_2 =(1-C^2/C_s^2)^{1/2}$$ (20.a,b)

where C_d and C_s represent the longitudinal and shear wave velocities, respectively.

For a stationary crack (C=0) under impact loading as well as under static loading, the velocity functions are expressed by

$$A_I(0) = A_{II}(0) =A_{IV}(0) = (\kappa+1)/4, \quad A_{III}(0) = 1$$ (21.a,b)

where κ depends on only Poisson's ratio ν, and is defined as $\kappa=(3-\nu)/(1+\nu)$ for plane strain, and κ =3-4 ν for plane stress.

The salient features of the dynamic J integral can be summarized as follows:
(i) It physically represents the dynamic energy release rate G (Nishioka and Atluri, 1983).
(ii) For the far-field path, it has the property of the path-independent integral (Nishioka and Atluri, 1983).
(iii) For the near-field path, it is practically invariant with the shape of the infinitesimal near-field path (Nishioka, 1994).

Therefore, in numerical analyses, only far-field integrals can be usually used to evaluate the values of the dynamic J integral. In this case it is convenient to use the following expression:

$$J'_k=\int_{\Gamma+\Gamma_c}[(W+K)n_k-t_iu_{i,k}]dS+\int_{V_\Gamma}[(\rho\ddot{u}_i-f_i)u_{i,k}-\rho\dot{u}_i\dot{u}_{i,k}]dV$$ (22)

7.2 Determination of mixed-mode stress intensity factors from the dynamic J integral components

At each iteration step and each time step in the moving finite element method explained in

9

Section 4, the global components of the dynamic J integral can be evaluated by using Eq.(22). The crack-axis components of the dynamic J integral can be converted from the global components of the dynamic J integral, using Eq.(15). Then substituting these values in Eqs.(16) and (17), the in-plane mixed-mode stress intensity factors K_I and K_{II} can be determined directly (Nishioka and Atluri, 1984).

Although this direct method itself is theoretically valid, some difficulty arises if the value of J'^0_2 obtained by a numerical analysis is not very accurate. For a dynamically propagating crack, the integrand (W+K) in the dynamic J integral possesses a singularity. Thus, if we use a moving singular element method incorporating the $r^{-1/2}$ stress singularity (Nishioka and Atluri, 1980a and b), the J'^0_2 integral is accurately evaluated. In this case, it is known that the direct method gives very accurate K_I and K_{II} values (see Nishioka and Atluri, 1986).

On the other hand, when ordinary non-singular elements are used in the vicinity of a crack tip, the evaluated values of J'^0_2 by non-singular elements may not be very accurate due to the lack of the singularity in the integrand $(W+K)n^0_2$ along the crack surface path Γ_C (see Eq.(22)), where n^0_2 is the x^0_2 component of the outward normal unit vector. When the integration point on the crack surface path Γ_C approaches the crack tip ($r\rightarrow 0$), the direction cosine n^0_2 behaves as $(n^0_2)^\pm\rightarrow\pm(-1)$. Thus, the singular integration theoretically known to exist along the crack surface path cannot be performed when non-singular elements are used around the crack tip.

Contrary to this, in the integration of J'^0_1, either the singular element or non-singular elements can provide accurate K_I and K_{II} values, since as the integration point on the crack surface path Γ_C approaches the crack tip ($r\rightarrow 0$), the integrand of J'^0_1, becomes zero due to $(n^0_1)^\pm\rightarrow 0$. In other words, the evaluation of J'^0_1 is not affected by the modeling of the crack tip, while the J'^0_2 is affected by the modeling of the crack tip.

In order to overcome the difficulty in the direct method, and to accurately evaluate the in-plane mixed-mode stress intensity factors from the dynamic J integral values, the component separation method has been proposed by Nishioka et al. (1990b). The formulae of the component separation method are expressed by using the global components of the dynamic J integral as

$$K_I = \delta_I \left\{ \frac{2\mu\beta_2(J'_1\cos\theta_0 + J'_2\sin\theta_0)}{A_I\left(\delta_I^2\beta_2 + \delta_{II}^2\beta_1\right)} \right\}^{1/2} \tag{23.a}$$

$$K_{II} = \delta_{II} \left\{ \frac{2\mu\beta_1(J'_1\cos\theta_0 + J'_2\sin\theta_0)}{A_{II}\left(\delta_I^2\beta_2 + \delta_{II}^2\beta_1\right)} \right\}^{1/2} \tag{23.b}$$

where δ_I and δ_{II} are the mode I and mode II crack opening displacements at a point near the crack tip. θ_0 is the angle of crack direction measured from the global axis X_1. If the crack-axis component J'^0_1 is obtained by Eq.(15), the following formulae are also useful:

$$K_I = \delta_I \left\{ \frac{2\mu\, J'^0_1 \beta_2}{A_I\left(\delta_I^2\beta_2 + \delta_{II}^2\beta_1\right)} \right\}^{1/2} \tag{24.a}$$

$$K_{II} = \delta_{II} \left\{ \frac{2\mu\, J'^0_1 \beta_1}{A_{II}\left(\delta_I^2\beta_2 + \delta_{II}^2\beta_1\right)} \right\}^{1/2} . \tag{24.b}$$

The component separation method has the following features: (i) mixed-mode stress intensity fractors can be evaluated by ordinary non-singular elements, and (ii) the signs of K_I and K_{II} are automatically determined by the signs of δ_I and δ_{II}, respectively.

8. Simulation Results

The initial mesh pattern for the impact fracture specimen with the loading eccentricity of e=0.0 is shown in Fig.14(a). The Delaunay automatic mesh generation was applied for the central part of

the specimen. The left and right end parts where no crack propagation is expected to occur are modeled by regular meshes. The total number of elements is initially 4325 with 2262 nodes.

The nodal points for the exterior boundary of the Delaunay automatic triangulation region are shown in Fig.14(b). The crack surfaces are separated by a small distance 2ε, as explained in Subsection 4.1. On the crack surfaces, pairs of two nodes are placed. In the crack tip region, the specified interior points are placed regularly with 30 points in the circumferential direction, and with 17 points in the radial direction. The size of the crack tip elements in the radial direction is 0.5mm.

As explained in Section 5, the velocity of the impact rod was imposed as $(\dot{u}_h) = 5$ m/s at the loading area as the initial boundary condition. The width of the loading area is considered to be 1mm on which three nodes are placed. Since the mass of the impact rod is about 10 times larger than that of the specimen, and since the acoustic impedance $(\sqrt{\rho E})$ of the rod is about 60 times larger than that of the specimen, the impact rod can be assumed to move rigidly with same velocity throughout the simulation. Also the body force in the specimen due to the gravity is neglected in this study.

8.1 Fracture-path prediction mode simulation

The mixed-phase fracture-path prediction mode simulations were carried out for the specimens with e=0.0 and 0.1. The plane stress condition was used. The crack propagation direction criterion was set to use the local symmetry ($K_{II} =0$) criterion. The time increment of $\Delta t=2\mu s$ was used throughout the simulations.

(1) Overall responses at the loading and support points

Firstly, the numerical results for the variations of the displacements at the loading point and the support points in the specimen of e=0.0 are shown in Fig.15. It is seen that at about 200 μs the left and right support points are separated from the supports. The variations of nodal forces at the loading points and support points are shown in Fig.16. It can be concluded from Figs.15 and 16 that the specimen was always pushed by the impact rod during the analysis. The load becomes the maximum (6000 N) at about 225 μs, while fairly small forces appear at the support points. Therefore, the behavior of this three-point bend specimen is very similar with that of a one-point bend specimen sometimes used in impact fracture tests.

The detailed responses of the support points are shown in Figs.17 and 18. In Fig.18, small reaction forces at the support points appear when the longitudinal wave induced by the impact load arrives at the supports (t=130.8 μs). These reaction forces become zero again at 180 μs. Then it is seen in Fig.17 that at this instant the support points start moving up from the supports.

For the case of e=0.1, although it is not shown here, the variation of the load is almost the same with that of e=0.0 shown in Fig.16. However the maximum load was 6400 N at 210 μs. The detailed variations of displacements and the nodal forces at the support points are shown in Figs.19 and 20. The impact longitudinal wave arrives earlier at the left support. At this instant (120.4 μs) small nodal reaction force appears at the left support point, then it becomes zero at 166 μs. Then the left support point starts moving up from the left support. Similar responses of the right support point occur with the delay of about 21 μs (the difference of the arrival times at the left and right supports) from those of the left one. It is interesting to see that the maximum reaction force at the left support point is about 45 N and that of the right one is about 25 N, and the average value 30 N corresponds with each support reaction force in the case of e=0.0 (see Fig.18).

(2) Simulated fracture path and dynamic fracture parameters

Using the local symmetry ($K_{II}=0$) criterion in the mixed-phase fracture-path prediction mode simulation, the simulated fracture path and the overall deformation at various instants are obtained and shown in Fig.21 for e=0.0. To clearly see the propagating crack, the deformation was magnified by 30 times. For the case of e=0.0, the dynamic fracture started at t=156 μs, as indicated in Fig.5. Thus, the crack was stationary until this time. The crack propagated straight toward the loading

11

point. As a consequence, the simulated fracture path is almost perfectly straight, as can be expected by the mode I loading condition of e=0.0. Thus the dynamic fracture path prediction was done successfully.

The non-contact situations at the support points can clearly be seen in the deformed specimen after 230 μs. As stated in the previous subsection, the separation of the support points from the supports started at 180 μs. However, in the deformed specimen at 210 μs, the separation at each support point is too small to be seen.

The simulated fracture path and the overall deformation for the specimen of e=0.1 are shown in Fig.22. In this case, the dynamic fracture started at t=120 μs. At the initiation of dynamic fracture, the crack kinked toward the direction where the local symmetry criterion (K_{II}=0 criterion) is fulfilled. Then the crack propagated toward the loading point.

The dynamic J integral was evaluated for five circular paths with the radii of 1.0, 2.0, 3.0, 4.0 and 5.0 mm from the crack tip. The dynamic J integral values at various instants of time are plotted against the path number, in Fig.23 for e=0.0, and in Fig.24 for e=0.1. In each case, excellent path independence can be seen for not only the stationary crack under impact but also the dynamically propagating crack. The average values of the dynamic J integral were used to evaluate various fracture parameters.

The variations of the stress intensity factors converted from the average values of the dynamic J integral using the component separation method expressed by Eqs.(24.a) and (24.b) are shown in Fig.25 for the specimen of e=0.0. In the figure, C_d and C_s indicate the arrival times of the longitudinal and the shear waves from the impact loading point to the crack tip, respectively. Also T_p indicates the initiation time of dynamic crack propagation. When the compressive longitudinal wave arrives at the crack tip, K_I becomes slightly negative. This means that the crack surfaces are compressed slightly. In this study, this weak contact of the crack surfaces was ignored allowing a small overlapping. The K_I becomes positive and increases when the shear wave arrives at the crack tip. The K_{II} values are completely zero throughout the simulation. Once again this indicate that the postulated criterion (K_{II}=0) is successfully fulfilled during the fracture-path prediction mode simulation.

The stress intensity factors were also evaluated by the sizes of the caustic patterns using a theory of mixed-mode dynamic caustics developed by Nishioka and Kittaka (1990). These are also plotted in Fig.25. The experimentally obtained stress intensity factors agree excellently with the simulated ones. However, after crack propagation, they somewhat differ from the simulated ones although both tendencies are similar. The numerical simulation reveals the theoretically known instantaneous drop in the K_I value (Nishioka and Atluri, 1980b) for the sudden increase in the crack velocity. Thus, the difference in the early stage of dynamic crack propagation can be attributed to the slower response of caustic pattern for the sudden change of the crack velocity.

The variations of the stress intensity factors in the specimen of e=0.1 are shown in Fig.26. In this case, the compressive longitudinal wave obliquely impinges to the crack tip. For this reason, both K_I and K_{II} appear when it arrives at the crack tip (see C_d in Fig.26). After that, the K_{II} increases up to the fracture initiation. Similarly to the case of e=0.0, the K_I starts increasing steadily when the shear wave arrives at the crack tip. At the one set of dynamic fracture, the mode II stress intensity factor was dominant, thus almost pure mode II fracture occurred in this specimen. This is also evident in the deformed shape of the specimen at 120 μs (see Fig.22). After the onset of dynamic fracture, the K_{II} values are completely zero, since the local symmetry criterion (K_{II}=0) is imposed. Once again, this indicates the success of the intended simulation. Furthermore, the simulated stress intensity factors are in excellent agreement with the experimentally obtained ones.

In both specimens, during dynamic crack propagation, the stress intensity factors K_I increase (see Figs 25 and 26) although the experimentally obtained crack velocities steadily decrease (see Figs.5 and 6). This implies that an increasing K_I does not necessarily cause crack acceleration. In fact, Takahashi and Arakawa (1987) and Arakawa et al. (1997) observed increasing K_I values for decreasing crack velocities in their experiments. The mechanism of the acceleration effect on dynamic propagation fracture toughness, which was one of the most important unsolved problems

12

in dynamic fracture mechanics, was recently elucidated by Nishioka et al. (2000). From the generation-phase simulation of the experiment of Arakawa et al. (1997), a linear relationship was found between the excess unsteady-tem stress $\Delta\sigma_{22}$ (the higher-order stress field for an unsteadily propagating crack (Freund and Rosakis, 1992 and Nishioka Kondo, 1995)) at 1 mm ahead of the crack tip and the rate of the dynamic propagating fracture toughness $\dot{K}_{ID}$. Also, it was found that, in the earlier stage of crack deceleration process, $\dot{K}_{ID}$ is positive and has a linear relation with the crack velocity $\dot{a}$. Therefore, in the earlier stage of crack deceleration, it is possible to observe the increasing stress intensity factor even for decreasing crack velocity.

8.2 Comparisons of different types of simulations

The generation phase simulation was also carried out for the case of e=0.1, using the experimental data of the crack propagation history and the fracture path history. The fracture path should exactly agree with the experimental fracture path, since the crack tip in this model was forced to move along the experimental one (see Fig.27).

Another mixed-phase path-prediction mode simulation was carried out for e=0.1, using the maximum hoop stress criterion as the propagation-direction criterion. The experimental and two simulated fracture paths up to t=210 μs are compared in Fig.27. The overall agreement of three fracture paths is excellent, as seen in Fig.27(a). The magnified view of the fracture paths is shown in Fig.27(b). The initial kinked angle obtained by the local symmetry criterion agrees excellently with the actual experimental one, while the initial kinked angle obtained by the maximum hoop stress criterion is smaller than the experimental one. The fracture path simulated by the maximum hoop stress criterion after $X_1 \geq 10$mm coincides with the actual fracture path. Contrary to this, the fracture path simulated by the local symmetry criterion starts to deviate after about $X_1 \geq 2.5$ mm, and after $X_1 \geq 10$mm the simulated fracture path becomes parallel to the actual one. However, it should be noted that the deviation of the two paths is very small and only 1.3mm.

The variations of the stress intensity factors obtained by the generation phase simulation are shown in Fig.28(a), while those obtained by the fracture-path prediction mode simulation with the maximum hoop stress criterion are shown in Fig.28(b). For the stationary crack $(0 \leq t \leq T_p)$, all variations of the mixed mode stress intensity factors K_I and K_{II} are the same (see Fig.26, Figs.28(a) and 28(b)). In all cases, it is remarkable to see that the crack deformation mode drastically changes from the mode II dominance to the mode I dominance, instantly after the onset of dynamic fracture. The K_I and K_{II} variations obtained by various types of simulations agree well each other. However, the K_{II} values obtained by the maximum hoop stress criterion exhibit somewhat oscillatory behavior.

9. Conclusions

In this paper, first, high-speed photographs of impact fracture phenomena were presented. From these photographs, detailed histories of dynamic crack propagation and dynamic fracture path were evaluated.

Next, the moving finite element method based on Delaunay automatic mesh generation was developed. Various numerical procedures for the mixed-phase simulation with path prediction mode were developed in conjunction with the numerical procedures in the moving finite element method. Also numerical procedures for the contact/non-contact conditions at the loading and support points were developed. The present method made it possible to investigate its validity of any physically described criterion for crack propagation direction.

Using the moving finite element method based on Delaunay automatic mesh generation, the mixed-phase path prediction mode simulations with the local symmetry criterion were carried out for the impact fracture experiments with the loading eccentricities of e=0.0 and e=0.1.

From the numerical simulations, detailed responses of the dynamically fracturing specimens were clarified.

The present method successfully predicted precise fracture paths in non-self-similar fast fracture phenomena such as dynamically kinking and curving crack propagation. In addition, the local

13

symmetry criterion was found to be useful as the propagation-direction criterion.

References

Arakawa, K. Nagoh, D. and Takahashi, K., 1997. Crack velocity and acceleration effects on the dynamic stress intensity factor in polymers, International Journal of Fracture, Vol.83, pp.305-313.

Bathe, K.J. and Wilson, E.L., 1976. Numerical Methods in Finite Element Analysis. Prentice-Hall, New Jersey.

Camacho, G.T. and Ortiz, M., 1996. Computational modelling of impact damage in brittle materials, International Journal of Solids and Structures, Vol.33, No.20-22, pp.2899-2938.

Erdogan, F. and Sih, G.C., 1963. On the crack extension in plates under plane loading and transverse shear. Journal of Basic Engineering, ASME, Vol.85, pp.519-527.

Freund, L.B. and Rosakis, A.J., 1992. The structure of the near-tip field during transient elastodynamic crack growth, Journal of the Mechanics and Physics in Solids, Vol.40, No.3, pp.699-719.

Goldstein, R.V. and Salganik, R.L., 1974. Brittle fracture of solids with arbitrary cracks. International Journal of Fracture, Vol.10, No.10. pp.507-523.

Kanninen, M.F., 1978. A critical appraisal of solution techniques in dynamic fracture mechanics, In: Numerical Methods in Fracture Mechanics, (D.R.J. Owen and A.R. Luxmoore, eds.), Pineridge Press, pp.612-634.

Nemat-Nasser, S. and Horii, H., 1982. Compression-induced nonplanar crack with application to splitting, exfoliation and rockburst. Journal of Geophysical Research, Vol.87, No.B8, pp.6805-6821

Nishioka, T. and Atluri, S. N., 1980. Numerical modeling of dynamic crack propagation in finite bodies, by moving singular elements - Part I. Formulation. Journal of Applied Mechanics, Vol.47, No.3, pp.570-576.

Nishioka, T. and Atluri, S. N., 1980. Numerical modeling of dynamic crack propagation in finite bodies, by moving singular elements - Part II. Results. Journal of Applied Mechanics, Vol.47, No.3, pp.577-582.

Nishioka, T. and Atluri, S. N., 1982. Finite element simulation of fast fracture in steel DCB specimen. Engineering Fracture Mechanics, Vol.16, No.2, pp.157-175.

Nishioka, T. and Atluri, S. N., 1983. Path independent integrals, energy release rates and general solutions of near-tip fields in mixed-mode dynamic fracture mechanics. Engineering Fracture Mechanics, Vol.18, No.1, pp.1-22.

Nishioka, T., Perl, M. and Atluri, S. N., 1983. An analysis of dynamic fracture in an impact test specimen. Journal of Pressure Vessel Technology, Vol.105, No.2, pp.124-131.

Nishioka, T. and Atluri, S. N., 1984. On the computation of mixed-mode K-factors for a dynamically propagating crack, using path-independent integrals J'_k. Engineering Fracture Mechanics, Vol.20, No.2, pp.193-208.

Nishioka, T. and Atluri, S. N., 1986. Computational methods in dynamic fracture, In: Computational Methods in the Mechanics of Fracture, (S.N. Atluri, Ed.), Elsevier Science Publishers, Chapter 10, pp.336-383.

Nishioka, T. and Kittaka, H., 1990. A theory of caustics for mixed-mode fast running cracks. Engineering Fracture Mechanics, Vol.36, No.6, pp.987-998.

Nishioka, T., Kittaka, H., Murakami, T. and Sakakura, K., 1990a. A laser caustic method for the measurement of mixed-mode dynamic stress intensity factors in fast curving fracture tests. International Journal of Pressure Vessels and Piping, Vol.44, pp.17-33.

Nishioka, T., Murakami, R. and Takemoto, Y., 1990b, The use of the dynamic J integral (J') in finite element simulation of mode I and mixed-mode dynamic crack propagation. International

Journal of Pressure Vessels and Piping, Vol.44, pp.329-352.

Nishioka, T., 1994. The State of the art in computational dynamic fracture mechanics. JSME International Journal, Series A, Vol.37, No.4, pp.313-333.

Nishioka, T. and Kondo, K., 1995. A unified derivation of explicit expressions for transient asymptotic solutions of dynamically propagating cracks under the mode I, II and III unsteady state conditions, Contemporary Research in Engineering Science, (R.C. Batra, ed.), Springer-Verlag, pp.393-417.

Nishioka, T., Nakatani, M., Okizuka, S. and Okada, T., 1996. Numerical simulations of self-similar and non-self-similar dynamic fracture phenomena, In: Proceedings of Asian Pacific Conference for Fracture and Strength, Kyongju, Korea, pp.699-704.

Nishioka, T., 1997. Computational dynamic fracture mechanics. International Journal of Fracture, Vol.86, No.1/2, pp.127-159.

Nishioka, T., Okada, T. and Nakatani, M., 1997. Mixed-phase simulation with fracture-path prediction mode for dynamically curving fracture. In: Advances in Fracture Research, Pergamon, Vol.4, pp.2063-2070.

Nishioka, T., Syano, S. and Fujimoto, T., 2000. A study on crack acceleration and deceleration effects in dynamic fracture phenomena, Advances on Computational Engineering and Sciences, (A.N. Atluri and F.W. Brust, editors), Volume I, Tech Science Press, Palmdale, CA, USA, pp.942-947.

Papadopoulos, G.A., 1988. Dynamic crack-bifurcation by the Det.-criterion.. Engineering Fracture Mechanics, Vol.31, pp.887-893.

Rice, J.R., 1968. A path independent integral and approximate analysis of strain concentration by notches and cracks. Journal of Applied Mechanics, Vol.35, pp.379-386.

Sih, G.C., 1972. Introductory chapter: a special theory of crack propagation. In: Mechanics of Fracture, Vol.1, Noordhoof, pp.XXI-XLV.

Sloan, S.W. and Houlsby, G.T., 1984. An implementation of Watson's algorithm for computing two-dimensional Delaunay triangulation, Advances in Engineering Software, Vol.6, 192-197.

Takahashi, K. and Arakawa, K., 1987. Dependence of crack acceleration on the dynamic stress-intensity factor in polymers. Experimental Mechanics, Vol.27, pp.195-200.

Taniguchi, T., 1992. Automatic Mesh Generation for FEM: Use of Delaunay Triangulation, Morikita Publishing.

Wu, C.H., 1978. Fracture under combined loads by maximum-energy-release-rate criterion. Journal of Applied Mechanics, Vol.45, pp.553-558.

Figure Captions

Fig.1 Three-point bend specimen for impact fracture

Fig.2 Fractured specimens

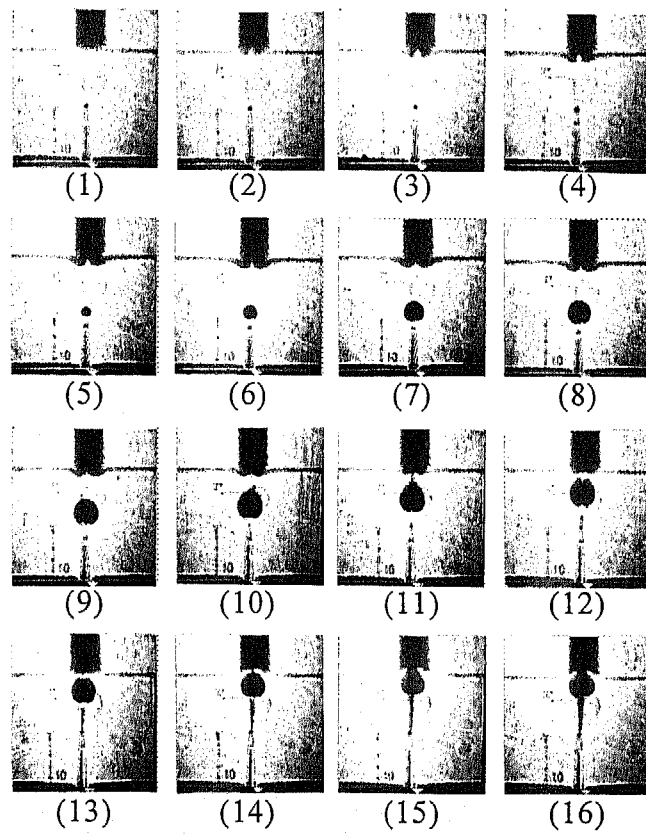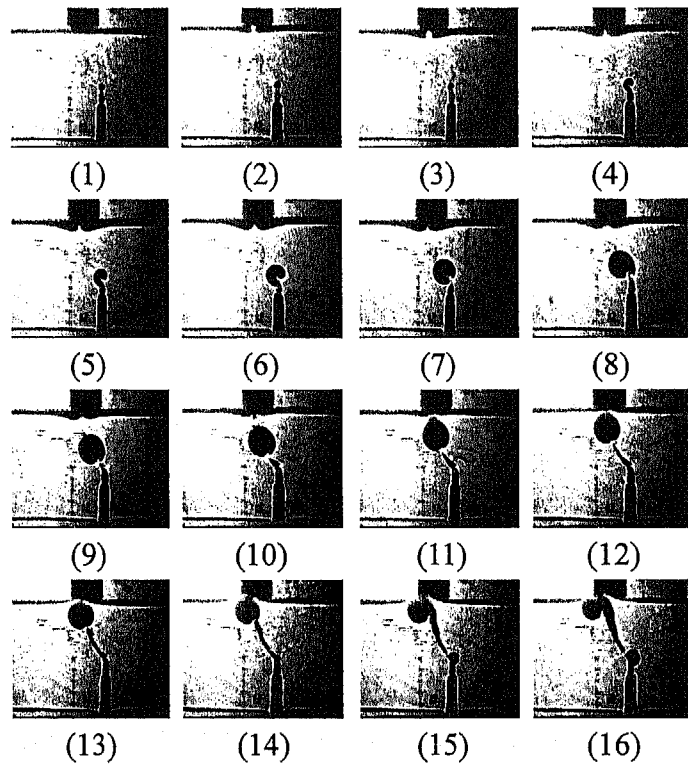Fig.3 High-speed photographs of dynamically fracturing specimen (e=0.0)

Fig.4 High-speed photographs of dynamically fracturing specimen (e=0.1)

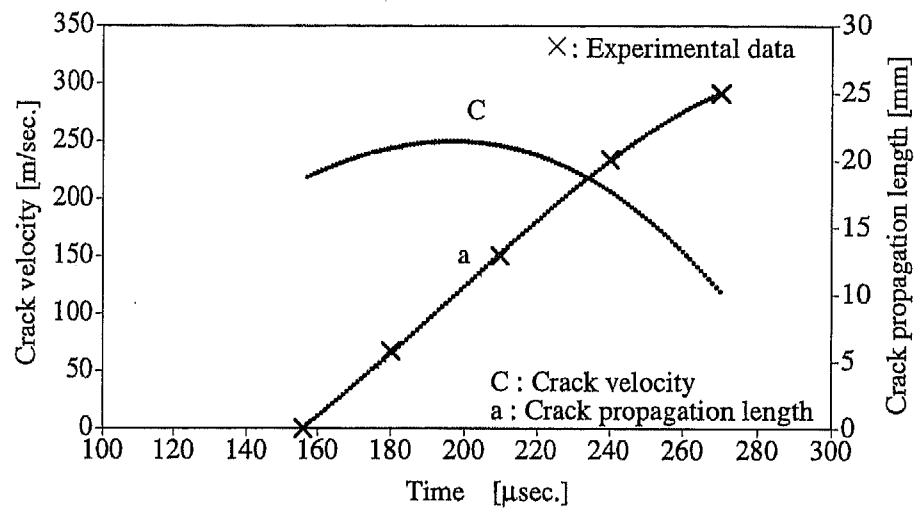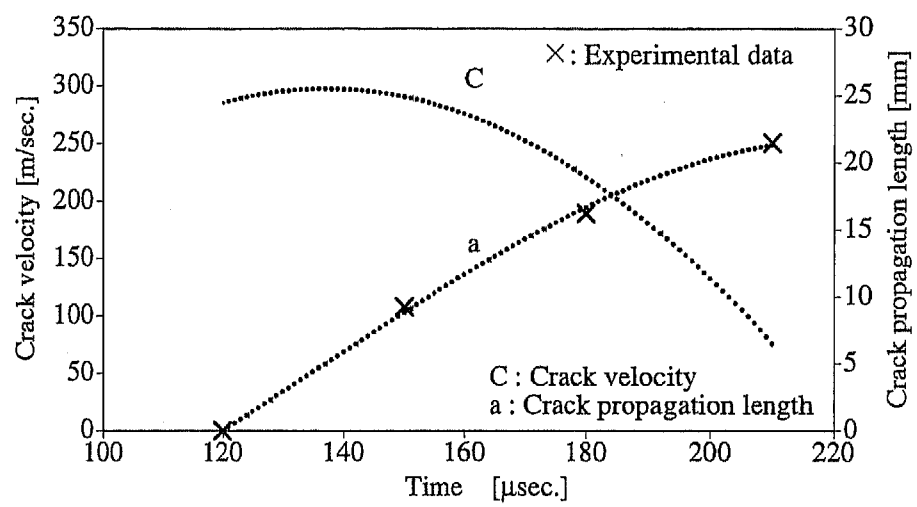Fig.5 Crack propagation history (e=0.0)
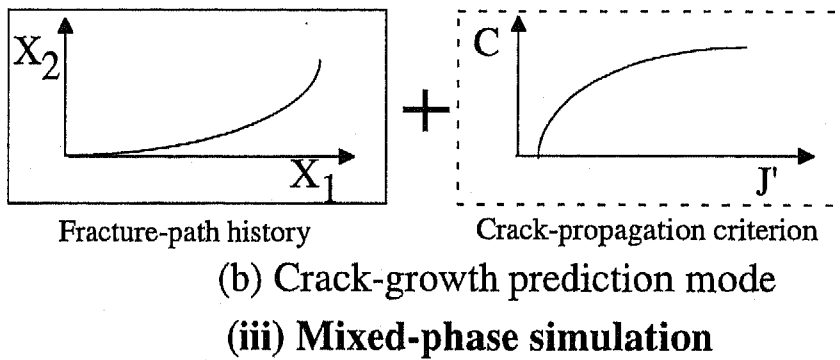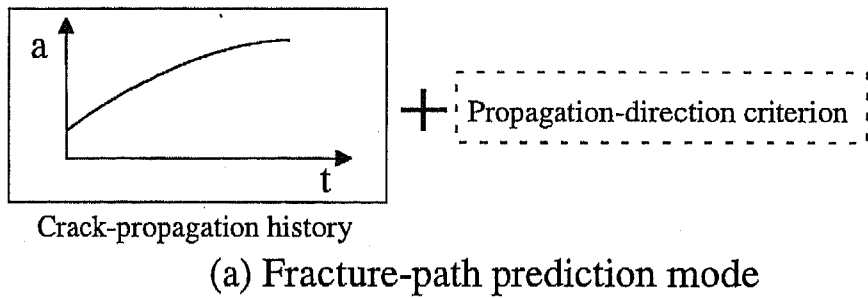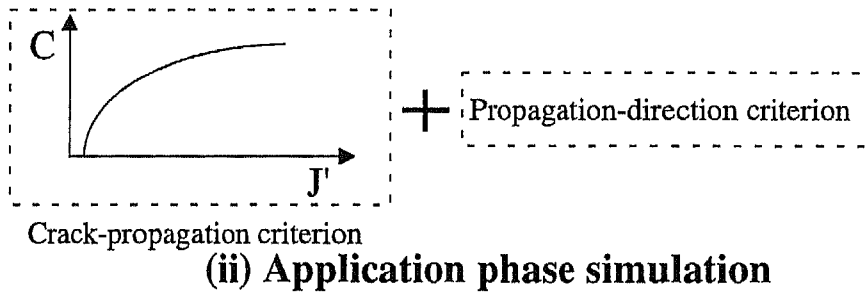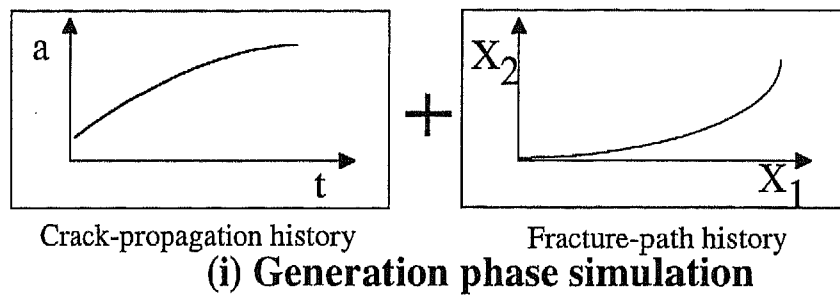
Fig.6 Crack propagation history (e=0.1)

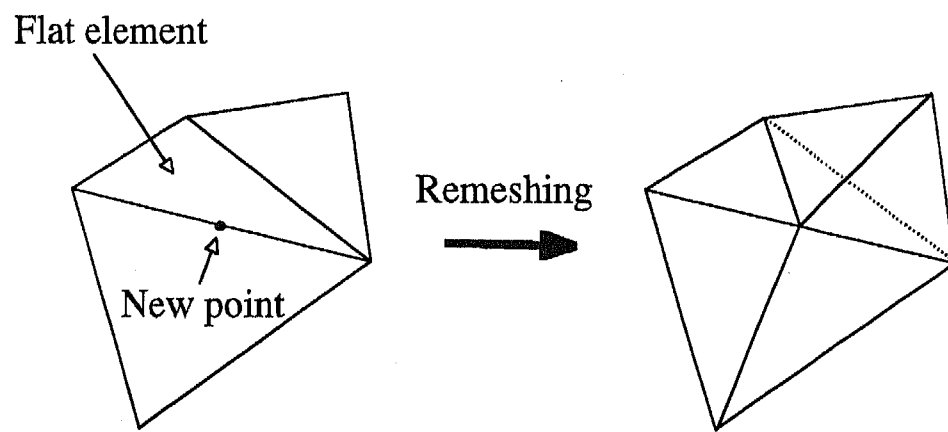Fig.7 Types of fracture simulations (Dynamic curving fracture)
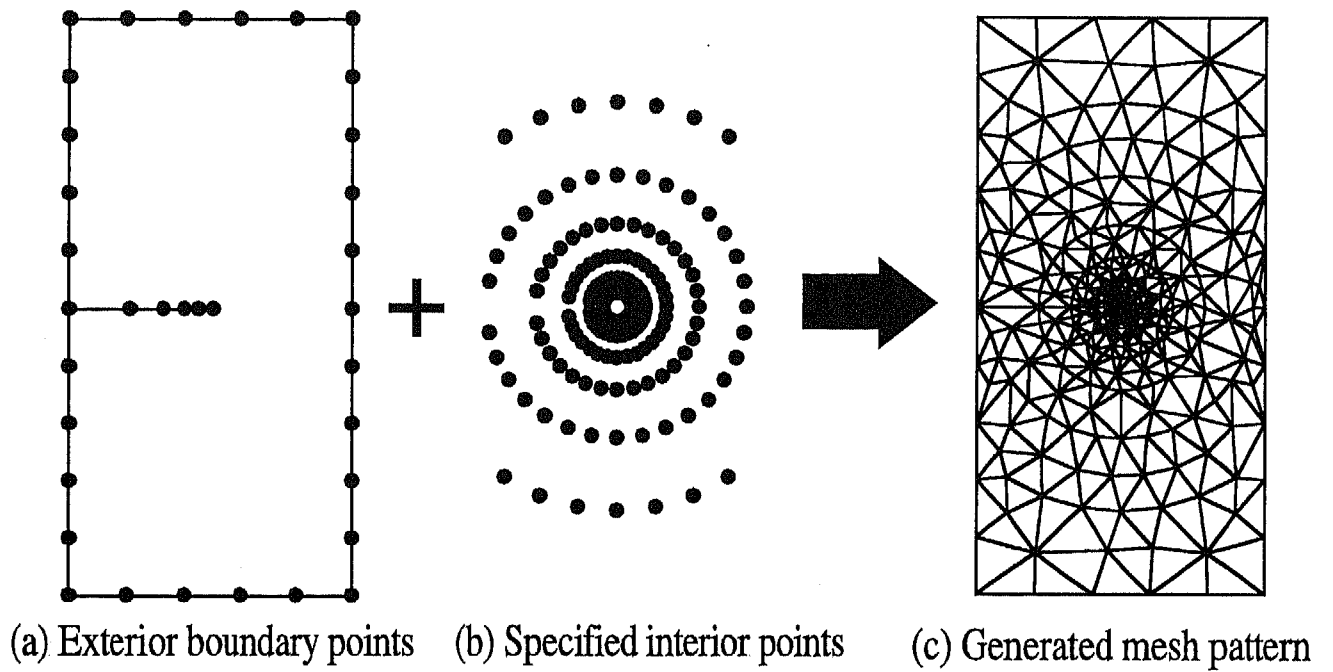
Fig.8 Remeshing procedure with the distortion rate
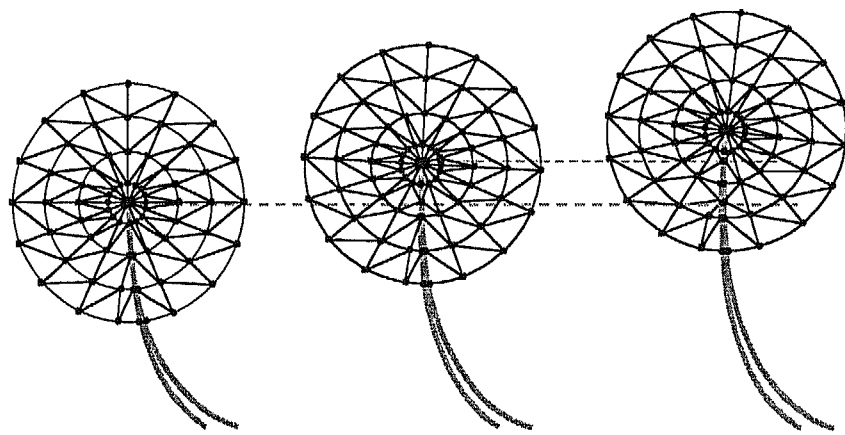
Fig.9 An example of automatic mesh generation

Fig.10 Moving elements around a propagating crack tip

Fig.11 A new nodal point in the previous mesh
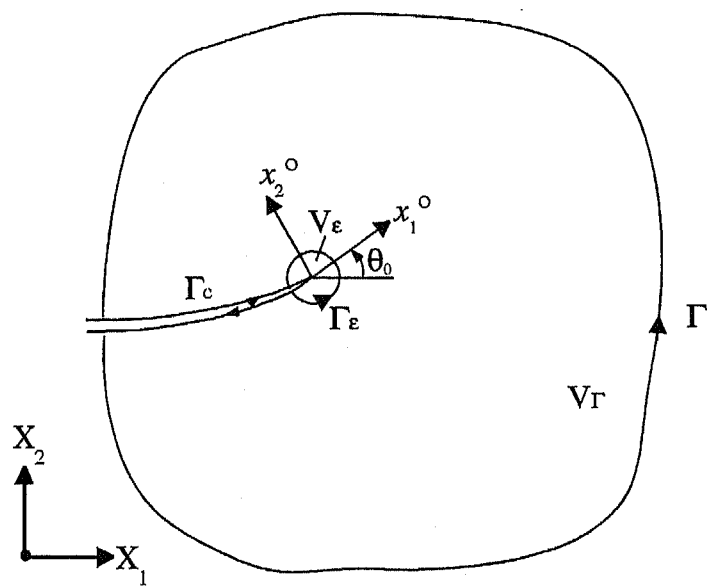
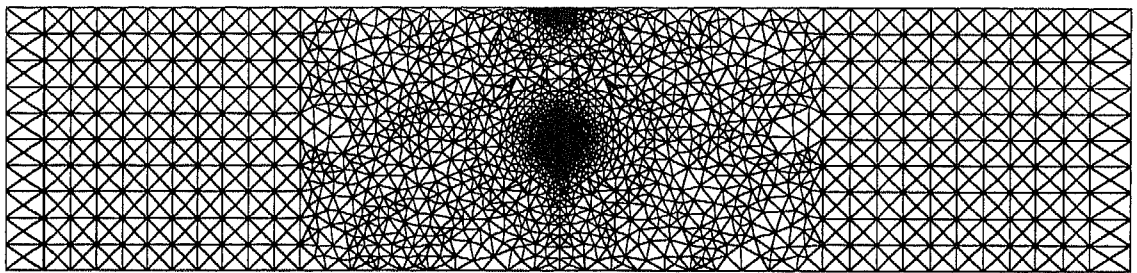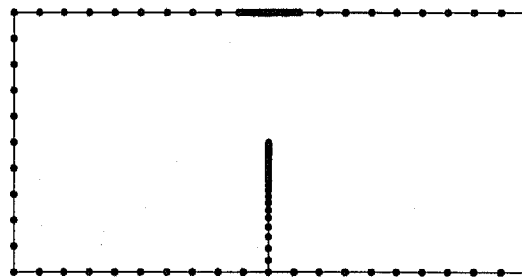Fig.12 Fracture path prediction procedure

Fig.13 Coordinate systems and integral paths
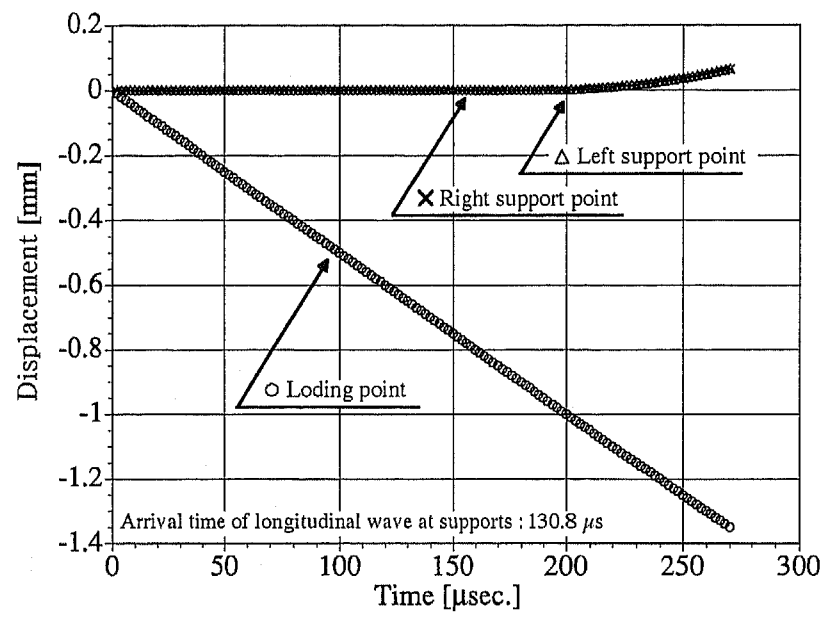
Fig.14 Initial mesh pattern for the impact fracture specimen

Fig.15 Variations of displacements at the loading and support points (e=0.0)
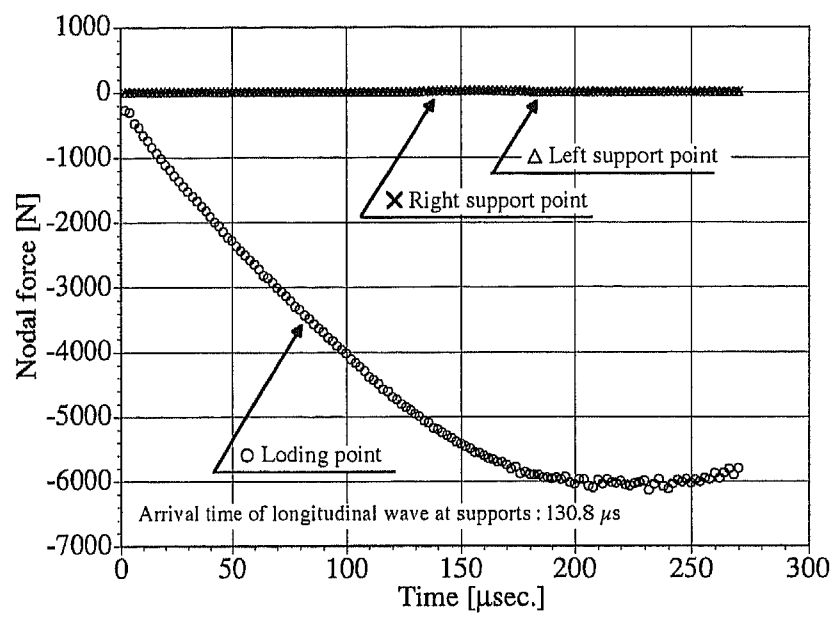
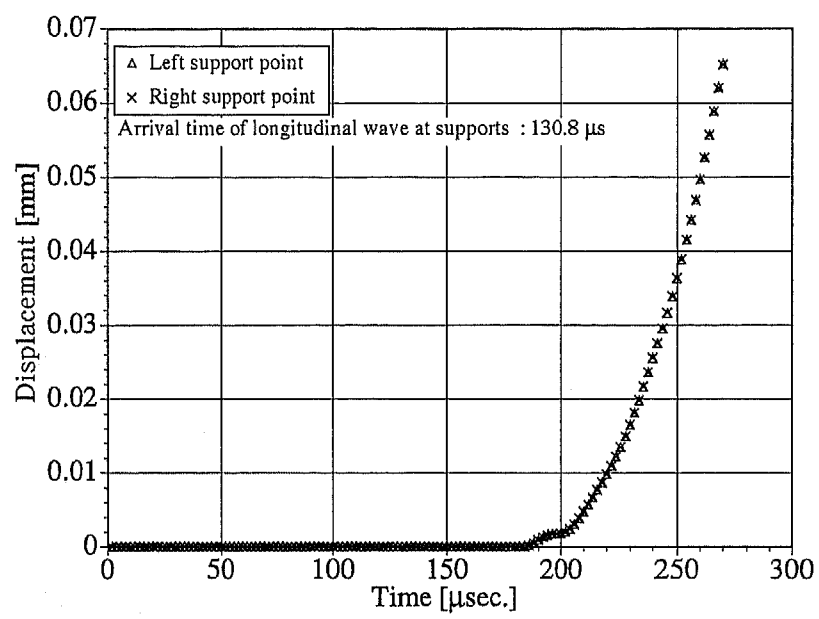Fig.16 Variations of forces at the loading and support points (e=0.0)

Fig.17 Displacements at the support points (e=0.0)
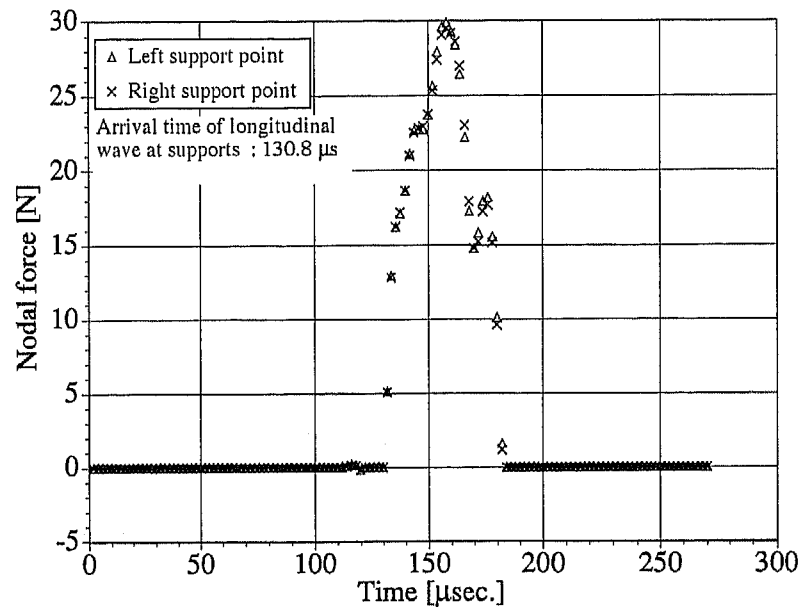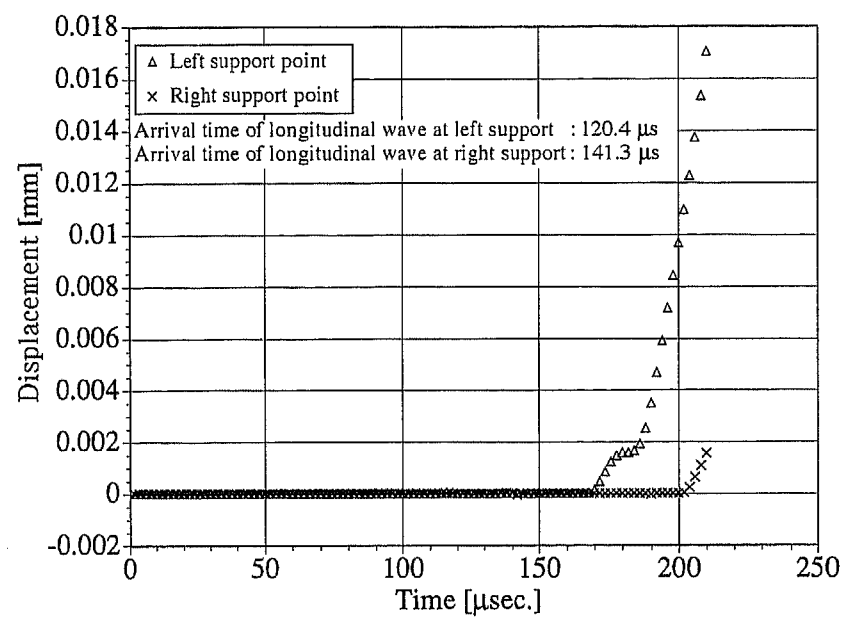
Fig.18 Forces at the support points (e=0.0)

Fig.19 Displacements at the support points (e=0.1)

Fig.20 Forces at the support points (e=0.1)

Fig.21 Simulation results for dynamic fracture path prediction with the $K_{II}=0$ criterion (e=0.0)

Fig.22 Simulation results for dynamic fracture path prediction with the $K_{II}=0$ criterion (e=0.1)

Fig.23 Dynamic J integral against path number (e=0.0, the $K_{II}=0$ criterion)

Fig.24 Dynamic J integral against path number (e=0.1, the $K_{II}=0$ criterion)

Fig.25 Dynamic stress intensity factors (e=0.0, the $K_{II}=0$ criterion)

Fig.26 Dynamic stress intensity factors (e=0.1, the $K_{II}=0$ criterion)

Fig.27 Comparison of fractured paths at 210 μs

Fig.28 Comparison of dynamic stress intensity factors (e=0.1)

Fig.1 Three-point bend specimen for impact fracture

Fig.2 Fractured specimens

Fig.3 High-speed photographs of dynamically fracturing specimen (e=0.0)

(1)   (2)   (3)   (4)

(5)   (6)   (7)   (8)

(9)   (10)   (11)   (12)

(13)   (14)   (15)   (16)

Fig.4 High-speed photographs of dynamically fracturing specimen (e=0.1)

Fig.5 Crack propagation history (e=0.0)

Fig.6 Crack propagation history (e=0.1)

Crack-propagation history   Fracture-path history

(i) Generation phase simulation

Crack-propagation criterion

(ii) Application phase simulation

Crack-propagation history

(a) Fracture-path prediction mode

Fracture-path history   Crack-propagation criterion

(b) Crack-growth prediction mode

(iii) Mixed-phase simulation

Fig.7 Types of fracture simulations
(Dynamic curving fracture)

Fig. 8 Remeshing procedure with the distortion rate

(a) Exterior boundary points   (b) Specified interior points   (c) Generated mesh pattern

Fig.9 An example of automatic mesh generation

Fig.10 Moving elements around a propagating crack tip

Fig.11 A new nodal point in the previous mesh

Fig.12 Fracture path prediction procedure

Fig.13 Coordinate systems and integral paths

(a) Initial mesh pattern

(b) Input data for exterior boundary

Fig.14 Initial mesh pattern for the impact fracture specimen (e=0.0)

Fig.15 Variations of displacements at the loading and support points (e=0.0)

Fig.16 Variations of forces at the loading and support points (e=0.0)

Fig.17 Displacements at the support points (e=0.0)

Fig.18 Forces at the support points (e=0.0)

Fig.19 Displacements at the support points (e=0.1)

Fig.20 Forces at the support points (e=0.1)

156 μs

170 μs

190 μs

210 μs

230 μs

250 μs

270 μs

Fig.21 Simulation results for dynamic fracture path prediction with
the $K_{II}=0$ criterion (e=0.0)

120 µs

130 µs

140 µs

150 µs

160 µs

170 µs

180 µs

190 µs

200 µs

210 µs

Fig.22 Simulation results for dynamic fracture path prediction
with the $K_{II}=0$ criterion (e=0.1)

Fig.23 Dynamic J integral against path number
(e=0.0, the K_{II}=0 criterion)

Fig.24 Dynamic J integral against path number
(e=0.1, the $K_{II}=0$ criterion)

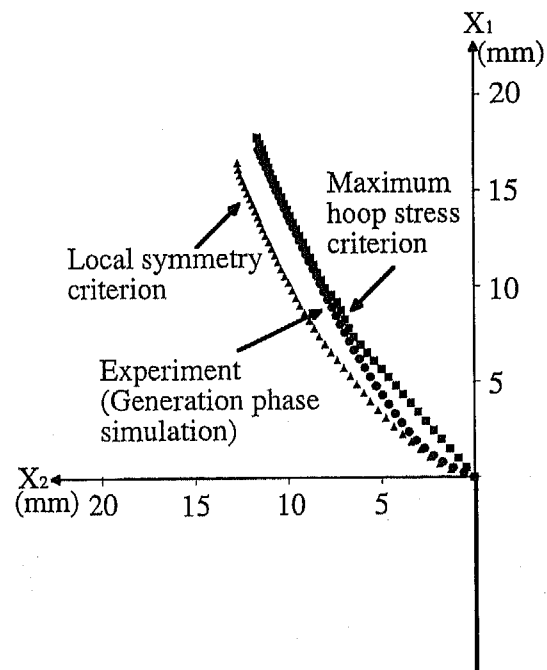Fig.25 Dynamic stress intensity factors
(e=0.0, the K_{II}=0 criterion)

Fig.26 Dynamic stress intensity factors
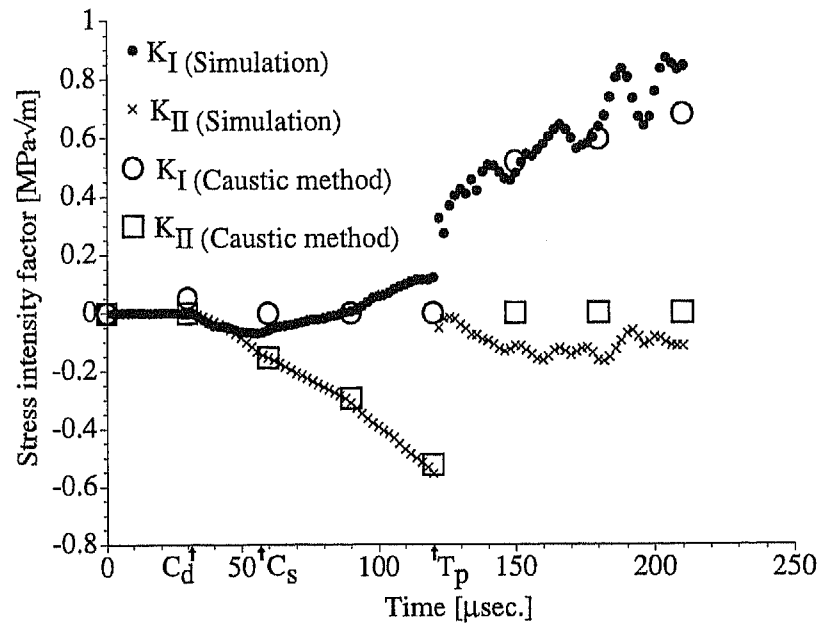(e=0.1, the K_{II}=0 criterion)

(a) Comparison of the experimental and simulated fracture paths

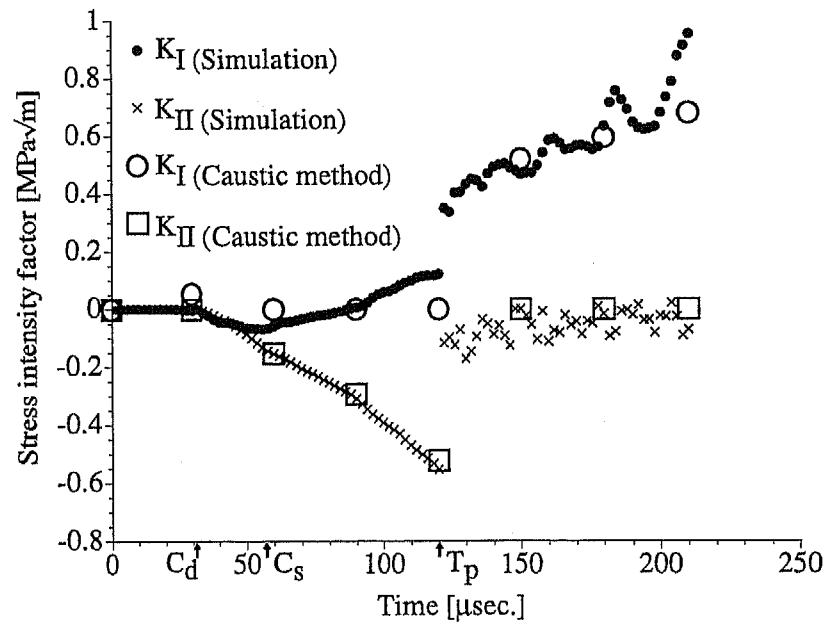
(b) Magnified view of the three fracture paths

Fig.27 Comparison of fractured paths at 210 μs

(a) Generation phase simulation

(b) Path-prediction mode simulation with
the maximum hoop stress criterion

Fig.28 Comparison of dynamic stress intensity factors (e=0.1)